Acoustic and aerodynamic evaluation of DLR small-scale rotor configuration within GARTEUR AG 26

Jianping Yin, F. de Gregorio, K.-S. Rossignol, L. Rottmann, G. Ceglia, Gabriel Reboul, G. Barakos, G. Qiao, M. Muth, M. Kessler, et al.

European Rotorcraft Forum

ACOUSTIC AND AERODYNAMIC EVALUATION OF DLR SMALL-SCALE ROTOR CONFIGURATIONS WITHIN GARTEUR AG26

J. Yin[1], F. De Gregorio[2], K.-S. Rossignol[1], L. Rottmann[1], G. Ceglia[2],
G. Reboul[3], G. Barakos[4], G. Qiao[4], M. Muth[5], M. Kessler[5]
A. Visingardi[2], M. Barbarino[2], F. Petrosino[2], A. Zanotti[6], N. Oberti[6]
L.Galimberti[6,8], G. Bernardini[7], C.Poggi[7], L. Abergo[6], F. Caccia[6]
A. Guardone[6], C. Testa[9], S. Zaghi[9]

1. German Aerospace Center - DLR, Braunscweig, Germany
2. Italian Aerospace Research Center - CIRA, Capua, Italy
3. French Aerospace Lab - ONERA, Chatillon, France
4. University of Glasgow, Scotland, UK
5. University of Stuttgart, Stuttgart, Germany
6. Politecnico di Milano, Milan, Italy
7. Roma Tre University, Rome, Italy
8. King Abdullah University of Science and Technology - KAUST, Saudi Arabia
9. CNR-INM, Rome, Italy

Abstract
This paper presents the activities performed in the GARTEUR Action Group HC/AG-26 to study the acoustic and aerodynamic characteristics of small rotor configurations, including the influence of the rotor-rotor interactions. This paper will focus on comparisons between numerical activities and wind tunnel results on a small rotor provided by DLR. The wind tunnel modelss included a Rotor/Rotor/Pylon in isolated, tandem and coaxial configuration. The wind tunnel experiments for acoustics were performed in DLR's Acoustic Wind Tunnel Braunschweig (AWB) and PIV test were performed in CIRA within a common CIRA/DLR test program. For simulations, the numerical approaches from each partner are applied. The aerodynamic simulations necessary for the aeroacoustic predictions are conducted with a range of fidelity numerical methods, varying from lifting line to CFD. The acoustic and aerodynamic predictions are compared to test data, including performance, PIV and acoustic directivity.

ABBREVIATIONS

D	Rotor diameter (0.33m)
f	Frequency (Hz)
p0	Air pressure in an undisturbed medium, Pa
rev	Revolution
T	Thrust in N
AWB	Acoustic Wind tunnel in Braunschweig
BPF	Blade Passing Frequency, Hz
FW-H	Ffowcs-Williams/Hawkings acoustic analogy
LHR	Left Handed Rotor
OASPL	Overall Sound Pressure Level, dB
PIV	Particle Image Velocimetry
RHR	Right Handed Rotor
ROI	Region of Interest
RPM	Rotor revolution per minute
SPL	Sound Pressure Level, dB

1. INTRODUCTION

Multirotor systems are increasingly applied to Vertical Take-Off and Landing (VTOL) configurations. Multirotor systems are popular for small-scale drones used for surveillance, monitoring, search, aerial surveying and photography, amongst other applications. In the context of a growing interest in the development of urban air mobility (UAM) solutions and providing answers to fundamental questions regarding the aerodynamic and acoustic characteristics of these new vehicles, the GARTEUR Action Group HC/AG-26[1] have been established. There are 14 partners involved in the group activities coordinated by DLR. The objectives of this AG are (1) to gain knowledge in noise generation and noise propagation of multirotor systems under the influence of the installation effects and (2) to develop and validate numerical prediction methods for the noise prediction for multirotor systems. For the purpose of the code validations, the results obtained by each partner were shared among the action group. Three data bases of test data were available from DLR[2][3], CIRA/CUSANO[4][5] and Polimi[6]. In addition, the first common test campaigns involving PIV measurement were carried out by CIRA/DLR[7], using the DLR small rotor configurations [2][3]. The common experiment aims at using the dedicated capabilities of the partner's wind tunnels to improve the validation database for the simulations and at the same time to validate the experimental accuracy by repeating the same experiments in several wind tunnels.

This paper will focus on the numerical comparison activities with the wind tunnel results involving only DLR small rotor configurations, including isolated

Presented at 49th European Rotorcraft Forum, Germany, 5-7th September, 2023

and rotor/rotor configurations. For the simulation of the various test cases, the numerical approaches from each partner are applied. The aerodynamic simulations necessary for the aeroacoustic predictions are conducted with a range of fidelity numerical methods, varying from lifting line to CFD. In the case of the acoustic installation effects, a scattering code can be applied or directly extract from CFD. The introduction of the experimental approach used in the acoustic/PIV test, including the rotor model, the instrumentation and the data reduction will also be presented. The methodologies applied in the numerical simulations by the partners will then be described and analyzed to point out their strengths and weaknesses. The aerodynamic and acoustic predictions will be analyzed and compared either code to code or with available test results for the different configurations considered. The acoustic results will be presented in terms of sound pressure level (SPL) directivities, spectra and sound pressure time histories.

2. DESCRIPTION ON THE ACOUSTIC AND PIV TEST SETUP

2.1. Acoustic test setup and measurement in DLR AWB

The AWB [8] is DLR's small-scale high-quality anechoic testing facility. It is an open-jet Göttingen-type wind tunnel capable of running at speeds of up to 65 m/s and optimized for noise measurements at frequencies above 250 Hz. The nozzle is 1.2 m high by 0.8 m in width. A special rig was designed to extend the capabilities of the facility to meet the requirements of simultaneous measurements of multiple rotors under static and flight conditions, e.g. Figure 1 and Figure 2.

The main objective of the selected mechanical design is to enable the investigation of the effect of flow and shaft angle on the acoustic radiation of a broad range of propeller configurations; isolated, coaxial, tandem with vertical and lateral offset, e.g. Figure 1. The dimensions of the AWB test section, allow the investigations of rotors with a diameter of up to approximately 0.4 m. The rig is designed to allow shaft angle variations in the range $\alpha \pm 30°$ and testing at free-stream velocities up to $U_\infty \approx 30\ \mathrm{m/s}$.

Figure 1 Experimental setup: single rotor (left), coaxial rotors (middle) and tandem rotors (right)

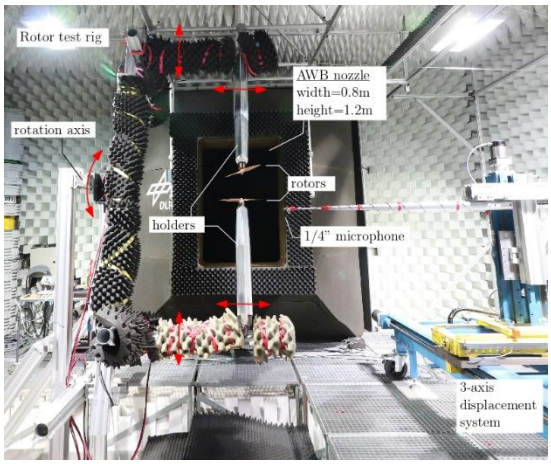

Figure 2 Overview of the full test rig and microphone setup installed in the AWB's test section. Center: coaxial configuration

Above $U_\infty \approx 30\ \mathrm{m/s}$, rig vibrations will have a noticeable influence on the loads, moments and acoustic measurements. Furthermore, the rig allows for lateral spacing settings in the range $\Delta y \pm 0.15\ \mathrm{m}$, streamwise spacing settings in the range $\Delta x \pm 0.3\ \mathrm{m}$ and vertical spacing settings in the range $\Delta z \pm 0.3\ \mathrm{m}$. These setting values are evidently valid for the current set of propellers considered herein. The whole structure of the rig is based on standard X-95 rails and carriers. This choice allows for easy changes in configuration. The rig is fixed to a rotating axle at its centre point, i.e. on the left-hand side of Figure 2 to allow variations in rotor shaft angle.

2.2. PIV test setup and measurement in CIRA

To characterize interactions in the flow field, isolated and multiple rotor configurations have been investigated in CIRA/DLR common tests, by means of standard two and three-component Particle Image Velocimetry measurement techniques. Several configurations have been investigated at Ω=8025, 10120 and 12000 RPM, respectively. Two propellers were investigated in tandem configuration by two

sCMOS double-frame cameras, characterized by 5.5 Mpx and 16bit pixels dynamic range. The cameras were equipped with 50 mm Canon EF focal lenses, and mounted on motorized rotating motors, allowing for camera rotation and for Scheimplugh correction.

The two cameras were installed side-by-side and horizontally oriented as shown in Figure 3, to increase the sizes of the measured region.

The measurement region was illuminated by a double-head Nd-Yag laser with a pulse energy of 150 mJ at a wavelength of 532 nm and a repetition rate of 10 Hz.

Figure 3 PIV set-up for tandem case in CIRA

The flow measurements provide a vector pitch of $\Delta x = 1.41mm$. The error of the PIV cross–correlation procedure is evaluated as 0.1 px as first estimation (Raffel et al.[9]). Using the current values for the optical resolution (11.3 px/mm) and the laser double–pulse delay (25-35 μs), this provides a velocity error of ΔV of ~ 0.25 m/s to 0.35 m/s. For a detailed description of the PIV measurement system, the reader is referred to the work of De Gregorio et al[7].

For the tandem configuration, the measured region covers between -2.13<x/R<0.29 along the radial direction and the area from slightly above the propeller disk until down to little more than two radii distance z/R=-2.1 (Figure 3, Figure 5-a). For the coaxial configuration, a different camera setup was adopted considering the presence of the fairing below the propeller blade. The PIV cameras were vertically mounted side-by-side (Figure 4) assuring a measurement region ranging along the x-axis between 0.16 < x/R < 1.3 and toward the z-axis down to z/R=-2.16 (Figure 5-b).

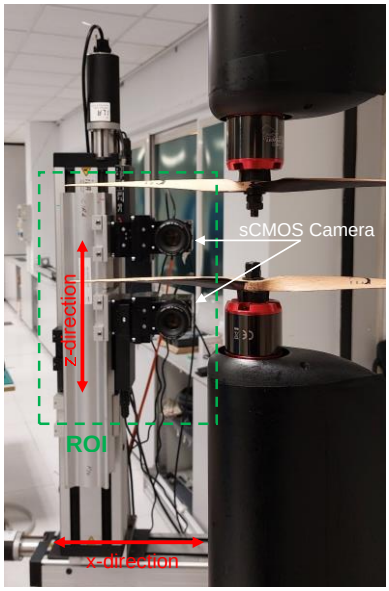

Figure 4 PIV set-up for coaxial configuration in CIRA

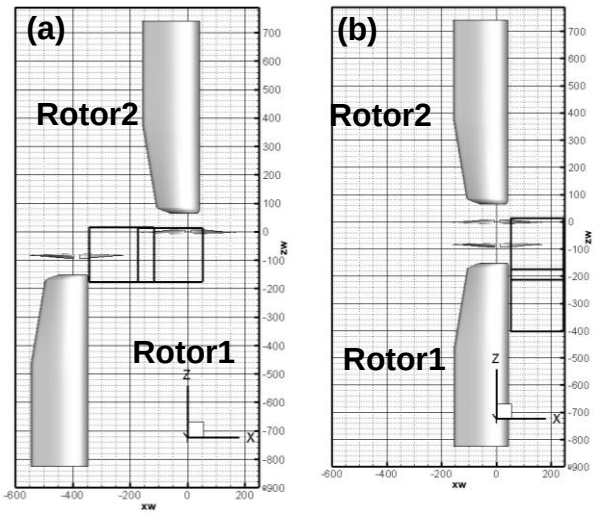

Tandem Δx=1.18 D and Δz=0.25 D

Coaxial: Δx=0 D and Δz=0.25 D

Figure 5 PIV set-up for two rotor case in CIRA

2.3. Rotor and Pylon

The rotor is a commercially available one ((Xoar model PJN). For this paper, the test results from a two-blade 13x7 rotor including a rotor support (pylon), as shown in Figure 6 are chosen for validating the numerical simulations. The rotor 13x7 represents a rotor with 13 inches or 0.33m in diameter and 7 inches in pitch. The rotor, pylon planform and the form of the section profiles are demonstrated in Figure 6. The twist and chord distribution are given in Figure 7 derived according to a scanned surface.

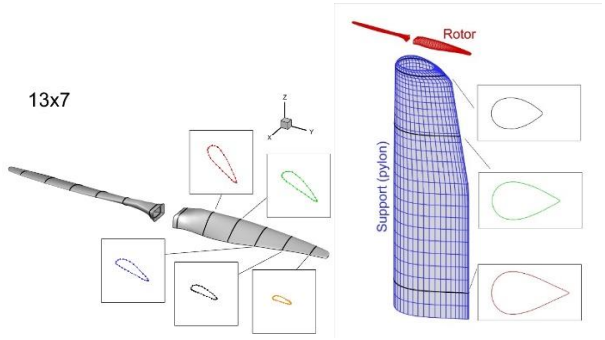

Figure 6 Rotor and pylon model

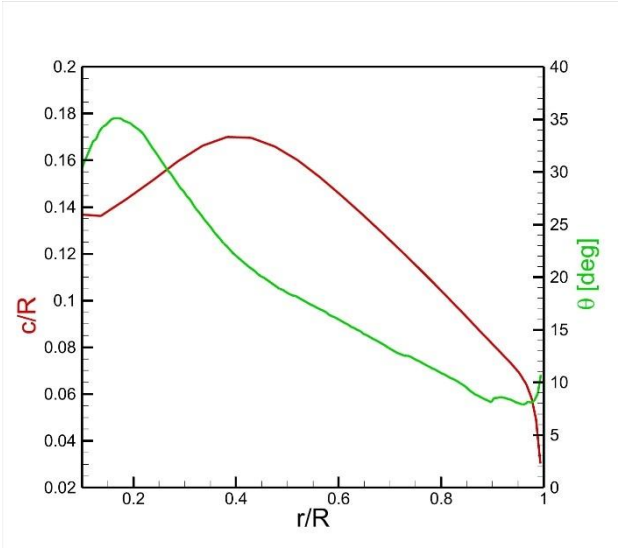

Figure 7 The twist and chord distribution

The rotors are mounted on Leopard LC5065 motors coupled to YGE 205HVT speed controllers and SM300-Series 3300 W DC power supplies. This combination allows RPM up to 13000 to be reached. For each rotor, performance data, in terms of thrust and torque, is acquired through miniature six-components load cells, Modell K6D40 from ME-Meßsysteme GmbH, mounted directly underneath the propellers. Each rotor RPM is acquired through a 1/rev signal generated by a Hall-effect sensor mounted to the rotor's shaft. This signal also serves as a trigger signal for data post-processing. Two multi-propeller configurations will be considered. An overview of these is given in Figure 5 a) and b). The so-named tandem configuration is defined by a relative position between the two rotor axes of $\Delta x=1.18$ of the rotor diameter D, $\Delta y=0$ and a vertical distance of $\Delta z=0.25D$. The coaxial configuration has Δx and Δy null, while the axial distance between the propeller disks is equal to $\Delta z=0.25$ D.

3. DESCRIPTION OF METHODOLOGIES APPLIED IN THE NUMERICAL SIMULATIONS BY THE PARTNERS

The numerical investigations are performed by each partner applying either in-house-developed or commercial computational tools. The aerodynamic simulations necessary for the aeroacoustic predictions are conducted with a range of fidelity numerical methods, varying from lifting line to CFD.

3.1. CIRA

The CIRA aerodynamic simulations were carried out by using the medium-fidelity code RAMSYS [10], which is an unsteady, inviscid and incompressible free-wake vortex lattice boundary element methodology (BEM) solver for multi-rotor, multi-body configurations developed at CIRA. It is based on Morino's boundary integral formulation [11] for the solution of Laplace's equation for the velocity potential φ. The surface pressure distributions are evaluated by applying the unsteady version of Bernoulli equation, which is then integrated to provide the forces and moments on the configuration and the surrounding obstacles. A computational acceleration is obtained by applying the module for symmetrical flows and geometries implemented in the solver and the parallel execution via the OpenMP API.
The ACO-FWH solver is used for computing the acoustic free-field generated by the rotor blades. It is based on the FW-H formulation [12] described in [13] [14] and [15]. The advanced-time formulation of Farassat 1A is employed, and the linear terms (the so-called thickness and loading noise contributions) are computed through integrals both on the moving blades surface (impermeable/rigid surface formulation). The computational acceleration is obtained by a parallel execution via the MPI API. The simulation of the aeroacoustic free-field was carried out by using the aerodynamic database evaluated by RAMSYS, and consisting of the rotor blade pressure distributions.

3.2. DLR

The free-wake panel method UPM [16][17] is based on a velocity-based, indirect potential formulation using a combination of source and vortex distribution on the solid surfaces and vortex panels in the wake. Compressibility effect of the flow is considered by applying the Prandtl-Glauert correction. The blade vortex interaction (BVI) is captured thanks to the free wake model used in UPM. The validation effort is supported by CFD TAU steady simulations on selected hover test cases. The unstructured CFD code TAU is based on the solution of the Reynolds averaged Navier-Stokes equations on hybrid unstructured meshes. The solver relies on a cell

vertex scheme to discretize the mass, momentum and energy fluxes [18]. Depending on the configurations, all interactions among propellers, rotor, fuselage, wings and tail are considered. By postprocessing the unsteady aerodynamic pressure on the blade surface, the Ffowcs Williams-Hawkings[32] (FW-H)-equation based code APSIM [19] is used to compute the noise radiation and to predict the acoustic levels on a given hemisphere surface.

3.3. ONERA

The aerodynamic simulations performed by ONERA are realized with the PUMA code [21]. PUMA (**p**otential **u**nsteady **m**ethods for **a**erodynamics) is an unsteady lifting line / free-wake solver developed at ONERA since 2013. It is built on a coupling between an aerodynamic module and a kinematic module. The aerodynamic module relies on a lifting line method with a free-wake model using the Mudry theory [20], which describes the unsteady evolution of a wake modeled by a potential discontinuity surface. The lifting line method relies on two-dimensional airfoils characteristics through lookup tables computed preliminary by CFD with the ONERA elsA1[1] code [22]. Some blade sweep correction and dynamic stall models are added. Concerning the kinematic module, it is based on a rigid multi-body system approach using a tree-like structure with links and articulations. It enables any arbitrary motion between the different elements. In order to speed up the computation the code has been parallelized using OpenMP and the Multilevel Fast Multipole Method has been implemented.

Concerning the numerical parameters used for the computations, they are based on previous experience. The lifting line is divided in 30 radial stations using a square root distribution. A time step of 5° was used over 25 rotor revolutions over which the last 6 are used for post-processing. The computations do not account for the rotor hub or other test rig components.

The unsteady spanwise distribution of loads obtained with PUMA are used as input for the KIM code [23][24] to determine the noise emission of the rotor thanks to a Ffowcs-Williams and Hawkings formulation implemented in a non-compact advanced time approach. Since only sectional forces are available and in order not to consider noise sources compact in the chord direction, the surface pressure is reconstructed over the entire blade thanks to interpolation based on the pressure distributions computed and stored during the airfoil polar computations.

3.4. Polimi

The single propeller case was simulated with both a mid-fidelity and a high-fidelity aerodynamics solver, respectively DUST and SU2. DUST is an open-source software developed by POLIMI to simulate the interactional aerodynamics of unconventional rotorcraft configurations. The code, released as free software under the open-source MIT license, relies on an integral boundary element formulation of the aerodynamic problem and on a vortex particle model of the wakes [25]. SU2 is an open-source toolkit distributed by the SU2 Foundation [27], freely available and licensed under the GNU Lesser General Public License. It uses the finite volume approach to solve partial differential equations (PDE) on unstructured meshes. It solves the Unsteady Reynold-averaged Navier-Stoke (URANS) equations to analyze typical aeronautical problems that involve turbulent flows in the compressible regime. Aerodynamic results obtained with both solvers are not trimmed. The aeroacoustic signature is computed by solving Ffowcs Williams-Hawkings[32] (FWH) equations. The surface pressure field on the propeller computed with the two solvers is provided as input to the same acoustic module [28]. The pylon for both DUST/SU2 simulations is not modelled.

3.5. Roma Tre University/CNR-INM (ROMA3)

The RM3 aerodynamic and aeroacoustic analyses rely on tools developed by the Roma Tre University unit in the last twenty years and widely validated in the past in helicopter and tiltrotor configurations [29][30]. The aerodynamic module is based on the boundary integral formulation for the velocity potential presented in [31], suited for helicopter configurations where blade-vortex interaction (BVI) occurs. This formulation is fully 3D, can be applied to bodies with arbitrary shape and motion, and allows the calculation of both wake distortion and blade pressure field. It assumes the potential field to be divided into an incident field, generated by doublets over the wake portion not in contact with the trailing edge (far wake), and a scattered field, generated by sources and doublets over the body and doublets over the wake portion very close to the trailing edge (near wake). This procedure allows one to overcome the instabilities arising when the wake comes too close to or impinges on the body. Recalling the equivalence between the surface distribution of doublets and vortices, the contribution of the wake portion experiencing BVI (far wake) is expressed in terms of thick vortex (i.e., Rankine vortices) distributions. The shape of the wake can be either assigned (prescribed-wake analysis) or obtained as a part of the solution (free-wake analysis) by a time-

[1] *elsA V4.2.01 Airbus-Safran-ONERA property*

marching integration scheme in which the wake is moved accordingly to the velocity field computed from the potential solution. Once the potential field is known, the Bernoulli theorem yields the pressure distribution on the body that, in turn, is used both to determine the aerodynamic loads and as an input to the aeroacoustic solver to predict the radiated noise. The aeroacoustic analysis is performed by a prediction tool based on the Ffowcs Williams and Hawkings equation (FWH) [32]. The solution of the FWH equation is achieved through the boundary integral representation known as the Farassat Formulation 1A [33].

3.6. Uni Stuttgart (IAG)

For high-fidelity simulation a framework consisting of FLOWer and ACCO was used at the Institute of Aerodynamics and Gas Dynamics (IAG) at the University of Stuttgart. CFD results are obtained with the block-structured code FLOWer, originally developed by DLR [34] and continuously extended at the IAG for rotorcraft and multirotor applications[35]. Acoustic coupling was provided by IAG's FW-H solver ACCO [36] which uses the transient flow data provided by FLOWer as an input.

FLOWer solves the three-dimensional, compressible RANS equations and enables unsteady flow solutions (URANS). The discretization of time and space is applied separately by the method of lines. For temporal discretization a second-order dual time stepping is used [37] with a time step of 0.5° to resolve acoustic waves, while for spatial discretization a 6th high-order weighted essentially non-oscillatory (WENO) scheme by Borges [38] is used. Furthermore, the k-omega turbulence model was applied to close the URANS equations. Using the Chimera technique separate meshes were created for the background and rotor, utilizing hanging grid nodes to reduce the numerical expense. The spatial resolution of a single rotor was achieved by 6.6 mio cells. The rotor surface was meshed with 144 cells in radial and 80 cells in chordwise direction with a refinement towards the blade tip, leading edge and trailing edge with cell sizes of less than one per mille of the radius. The rotor mesh is extruded in wall normal direction with 52 cells. The first surface cells satisfy $y+ < 1$ and an extrusion up to cell sizes corresponding 10% of the chord length is applied. The spatial discretization in the background mesh was based on the resolution of the first harmonic wave length, with 15 cells discretizing the wave length of the blade passing frequency (BPF).
The acoustic code ACCO is an in-house code of the IAG, which uses an acoustic integration surface for the generation of sound emissions. For the integration either the physical surfaces or a permeable surface surrounding the object of interest can be used. For the performed simulations, the physical blade data of 4 full rotor revolutions are used and the integration is achieved through the physical surface of the rotor blade, which includes all tonal sound sources.

3.7. UoG (University of Glasgow, Glasgow)

Helicopter Multi-Block (HMB3) code is employed in this study. The solver can accurately predict the aerodynamic performance, acoustics of propagation, and has been widely used in the investigation of rotorcraft flows [41], helicopter rotor aeroelasticity [42], and missile trajectory prediction [43]. Moreover, a good agreement when compared to experimental results in aerodynamics, acoustics and aeroelasticity of propellers, which can be seen in previous study [44]. Most recently, its ability to capture the interactions of multi-rotor flows and ducted propeller flows was documented [45]. HMB3 solves the Unsteady Reynolds Averaged Navier-Stokes(URANS) equation in integral form using the Arbitrary Lagrangian-Eulerian formulation for time-dependent domains, including moving boundary layers. HMB3 uses a cell-centred finite volume approach to discrete Navier-Stokes equations on multi-block, structured grids. The 3rd order MUSCL (Monotone Upstream-centered Schemes for Conservation Laws) approach is applied to provide high-order accuracy in space. In the present work, simulations are performed with the k−ω shear stress transport (SST) [46]turbulence model.
Regarding acoustics, the present work estimates the near-field information derived from pressure fields computed with the high-fidelity HMB3 tool. The sound pressure signal was obtained by subtracting the time-averaged pressure from the time-dependent data. All CFD grids are designed to have at least 20 cells in the near-field region to capture the target wavelength, which is calculated based on four times the Blade Passing Frequency (BPF = 400 Hz). approach has also been applied in previous work by Smith [47].

3.8. Summary

The numerical methodologies used in the group are summarized in Table 1.

Partner	Code	Description
CIRA	RAMSYS, ACO-suite	Unsteady, inviscid and incompressible free-wake Boundary Element Method (BEM), Ffowcs Williams /Hawkings (FW-H)
DLR	UPM, TAU APSIM	Free Wake Panel method, unstructured CFD, FW-H

ONERA	PUMA, KIM	Unsteady lifting line / free-wake solver, FW-H
Polimi	DUST, SU2	Free Wake Panel method and unsteady, compressible (URANS) CFD, FW-H
RomaTre University	RM3	Free wake boundary element method (BEM) + FWH
Uni Stuttgart	FLOWer, ACCO	Flower: unsteady, compressible (URANS) CFD solver with Chimera technique, Ffowcs Williams-Hawking Solver with source-time dominant algorithm
UoG	HMB3-HFWH	HM3 CFD solver, FW-H coupled with HMB3

Table 1 Main Characteristics of the codes used by the partners

For a mid-fidelity aerodynamic tool based on potential formulation and free wake, the specific number of panels on the blade and pylon utilized in this paper is listed in Table 2. The numbers are derived according to the convergence of the code results.

Partner	**Panel per Blade**	**Panel per Pylon**	**Time step ISO/Multi**	**Num. of revs ISO/Multi**
DLR UPM	1624	1470	5°/2°	16/8
CIRA RAMSYS	1450	1392	2°/2°	9/9
ONERA PUMA	N.A.	No Pylon	5°/5°	25/25
Polimi DUST	1050	No Pylon	3°/3°	15/15
ROMA3 RM3	3150	No Pylon	3°/3°	20/20

Table 2 Summary of the numerical resolution for mid fidelity aerodynamic tool used by the partners

The summary of CFD grids utilities is given in Table 3.

Partner	**Grid Cells Rotor (Million)**	**Grid Cells Total ISO/Multi (Million)**	**Time step ISO/Multi**	**Num. of revs ISO/Multi**
DLR TAU	N.A	34.2	stationary	stationary
IAG FLOWer	6.6	14.3/24	0.5°/0.5°	25/25
Polimi SU2	15	30	1°/1°	20/20
UoG	4.7	18.3	1°/2°	10/10

Table 3 Summary of CFD grids used by the partners

4. RESULTS FOR THE ISOLATED ROTOR

4.1. Hover at RPM= 8000, 10000,12000

4.1.1. Aerodynamic performance

A comparison of the measured and simulated time averaged rotor thrust and torque is given in Figure 8. No trim is applied in all simulations. Figure 8 indicates that general tendencies captured in the measurements are reproducible using all computational tools. The differences from the test results are very much depending on the accuracy of the solvers. For example, the most of the mid-fidelity code underpredicts the torque values due to the neglection of viscosity effects. The higher order of accuracy is obtained by all CFD code except DLR TAU which underestimated the value. The choice of a vortex core model as well as a vortex core radius can have an influence on the inflow downwash velocity and therefore rotor thrust. For CFD-related methods, the proper choice of grid resolutions is key to the rotor vortex with less dissipation or dispersion errors. For this rotor, flow separations were observed in CFD results.

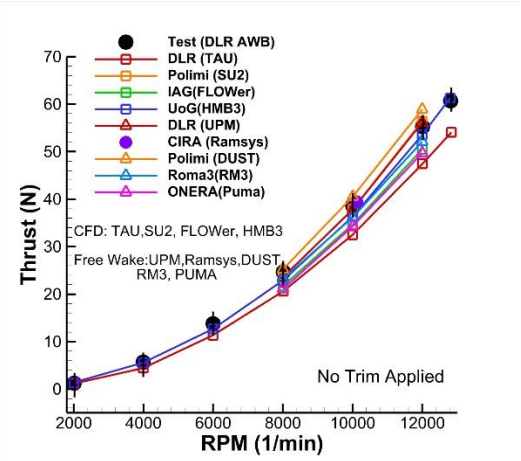

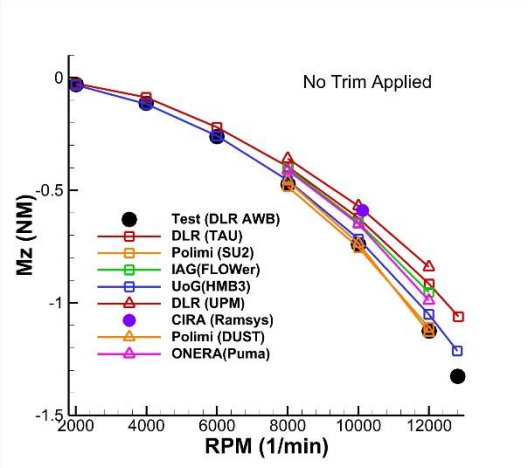

Figure 8 Time averaged rotor thrust and torque for 8000, 10000 and 12000 RPM

The comparison of the blade surface pressure distribution represented as pd=p-p0 (unsteady surface pressure) among the codes is given in Figure 9 for RPM 10000. The p0 is air pressure in undisturbed medium. The difference among the codes can be clearly observed especially in the blade tip region, which will be reflected in the noise value.

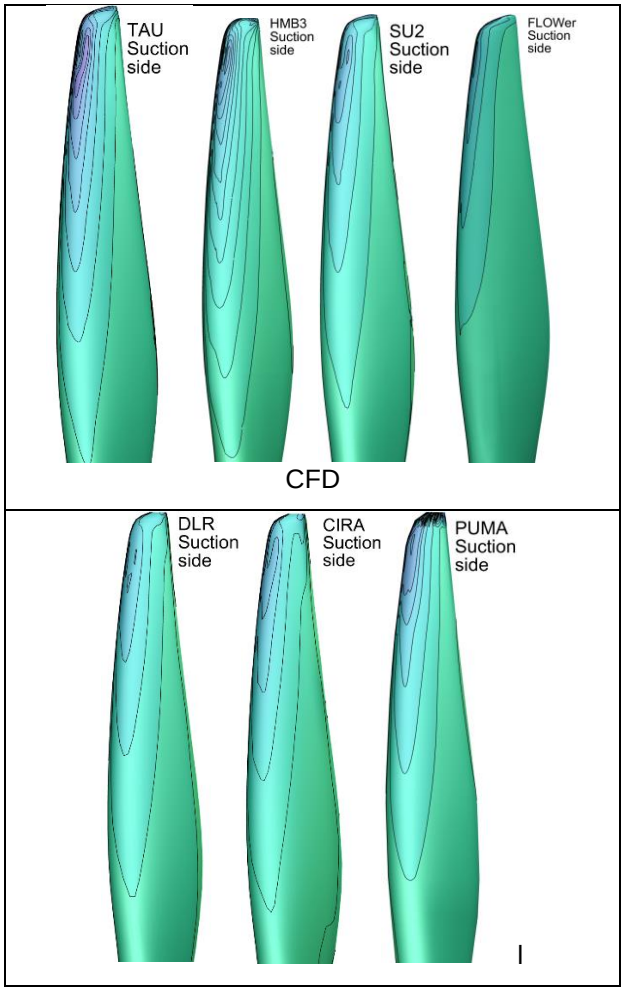

Free wake

Figure 9 Suction and pressure side distribution of the p-p0 at rpm 10000

4.1.2. Ensemble Average Velocity Fields

The simulated flow field behaviour is compared with ensemble average velocity fields obtained on 500 instantaneous velocity fields measured by the PIV technique[7] as shown in Figure 10 for isolated rotor at 10120 rpm.

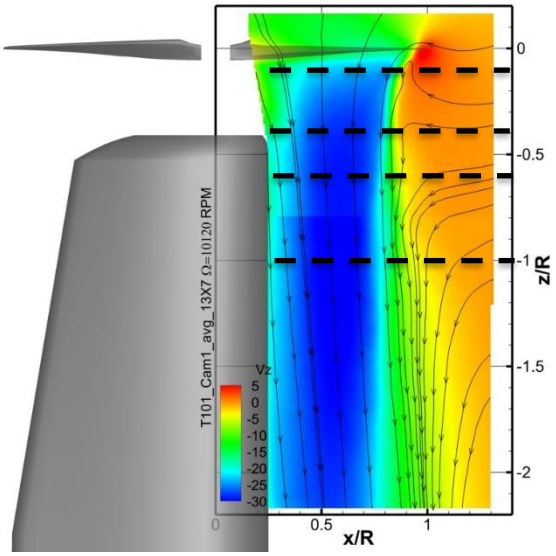

Figure 10 Iso-contours with streamtraces of the ensemble-average flow field colour-coded with the velocity vertical component at at Ω = 10120 RPM

The vertical velocity colour map, together with the stream traces, provides an overview of the flow field behaviour. The mean velocity shows the typical wake contraction immediately downstream of the rotor disk. To have quantitative comparison of PIV data, the comparisons are conducted on several slices at different Z positions marked as dashed line in the plot. Only vertical velocity is compared.

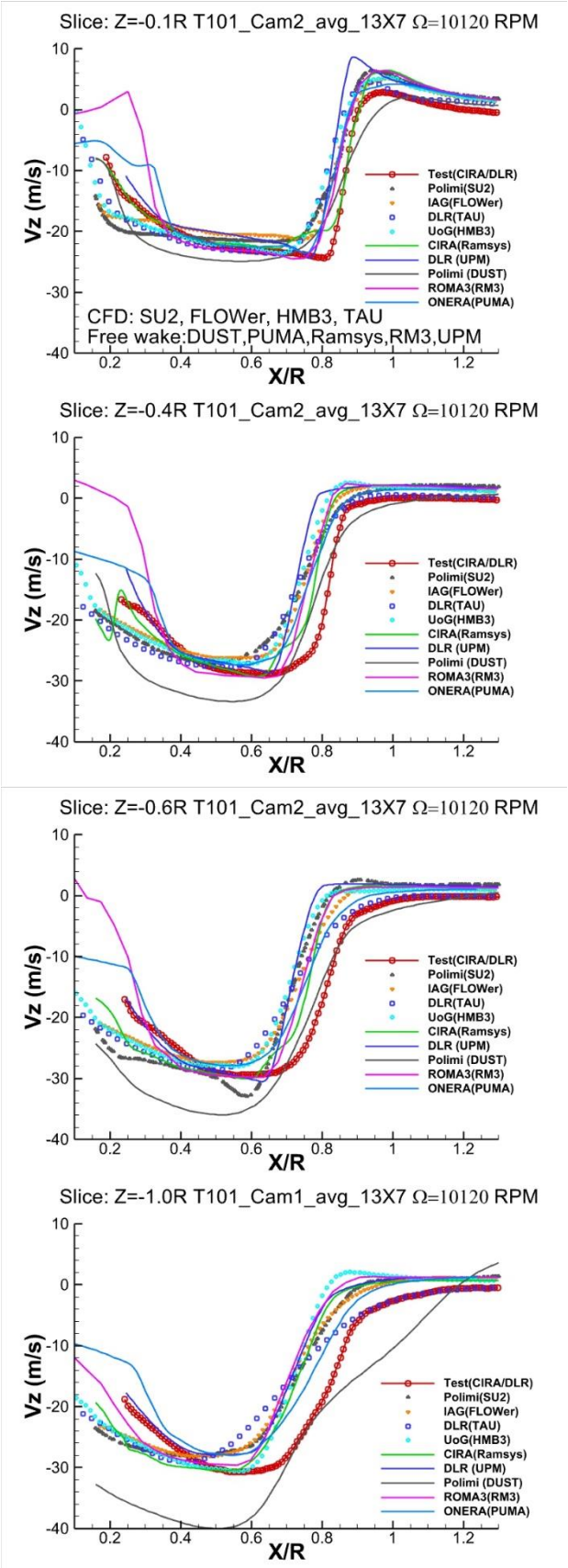

Figure 11 Vertical velocity trend along radial distance at Ω = 10120 RPM for different z-stations

Figure 11 shows that general forms, wake contraction and flow acceleration down to z = -1 R in the measurements are captured by most of computational tools. The comparisons are reasonably satisfactory. The Polimi DUST results exhibit possible a small dissipation model applied in the vortex development, therefore the velocity induced are very high. The results differ from other partners in large downstream position.

An interesting result is obtained in terms of the shear layer region location. Indeed, all simulations predict, more or less, the same position of the shear layer, which is different from the experiment. There is underestimation of the downward velocity in shear layer area. This means that the difference is independent of the simulation methodology used. The reason for it, is not very clear.

The difference in the area below the rotor hub occurs mainly from free wake potential code results where the hub is not modelled. Therefore, root vortex from free wake code can cause more deceleration on the flow in this area. Actually, RAMSYS and UPM results are closer to the experiment in this area. This is because the root vortex is annihilated in hover conditions. This looks a correct modelling solution. CFD results demonstrated in general similar characteristics to other results. In addition, in ONERA, UoG and ROMA3 results, as well as DLR and UoG CFD, the wind fairing Pylon is not included for the calculation, therefore large difference occurs in the root area.

4.1.3. Aeroacoustics

The presentation of the acoustic results will focus on data taken in the test on a polar arc represented by microphones from number 5 to 11 as defined in Figure 12. The arc is located in the Y-Z plane with an arc radius of 0.3m and polar angle difference of 15°. The microphone 9 is located in the rotational plane (X-Y), where Z=0. FW-H formulation is used by all partners.

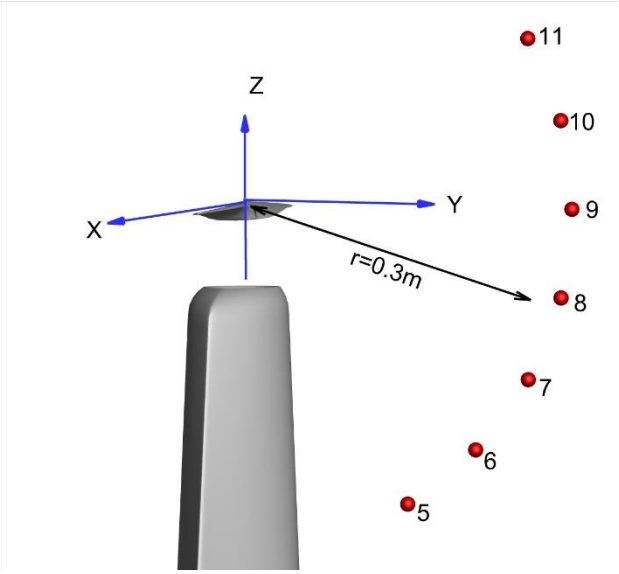

Figure 12 Microphone positions for the isolated rotor case.

The polar directivities for the overall sound pressure level derived from microphones 5 to 11 are shown for the isolated 13x7 rotor in Figure 13. The overall sound pressure levels obtained from the test using two averaging techniques are also included. The advantage of the time-averaged noise spectrum in one rotor revolution is that the random or stochastic noise sources, such as broadband noise can be removed or reduced dramatically. For the spectrum averaging technique, the spectrum is first obtained from the time series data blocks of each rotor revolution, then averaged to obtain a mean spectrum. The comparison indicates that the acoustic simulation results are able to capture the experimental trends for all the simulation. The higher loading noise contribution for the microphone above the rotor were predicted for all partners. Very large difference occurring at microphone 5 is because the microphone five is located directly below the rotor and the rotor downwash increases the microphone self-noise, which is not simulated. In general, the contribution of the broadband noise to the OASPL is negligible in the measurements.

The noise directivity calculated by DLR, IAG and ONERA shows very good agreement. Here the comparisons involve two fidelity levels. The agreement indicates that the wake had no great influence the main noise contribution came from the loading noise, which may occur for different fidelity levels. The Polimi results closest to the experimental data, while the results ROMA3 and UoG show agreement with others.

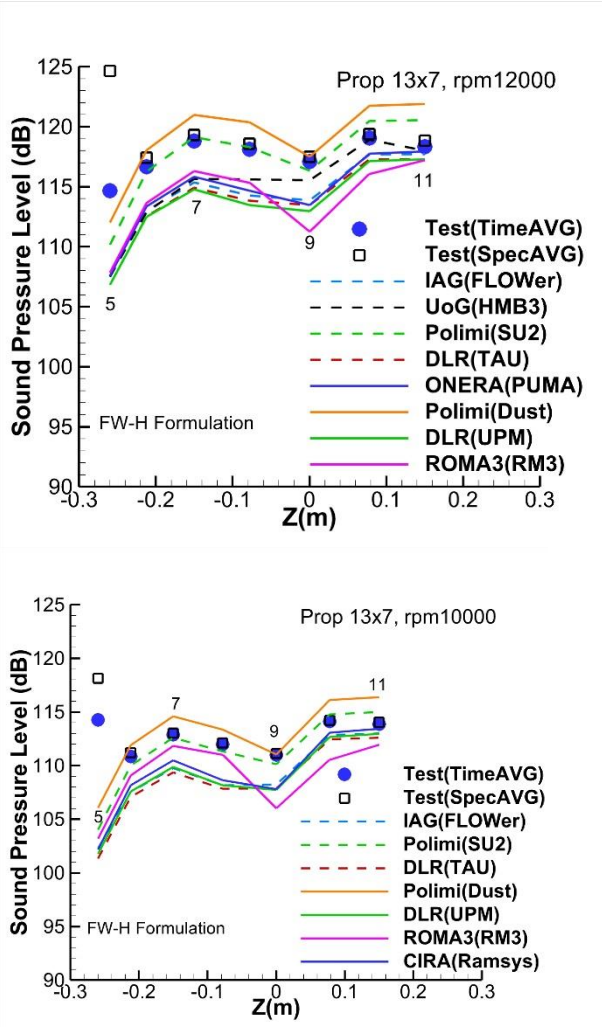

Figure 13 OASPL polar directivity taken from Mic 5 to Mic 11) for RPM 12000 and 10000

A more detailed data interpretation should be based on an examination of the sound pressure level (SPL) spectra or the time history. The acoustic results in terms of time histories at Mic. position 9 are compared, as shown in Figure 14. Figure 14 top shows a comparison of the predicted sound pressure time history at microphone 9 for rotor thickness noise. The thickness noise (Mono) from DLR and IAG predictions are perfectly meet, while the difference for Polimi indicate the influence of geometric discrepancy from both DLR and IAG.

The time history data from experiment in Figure 14 low exhibits high and low frequency variations. The low frequency 2-P variations are stronger than the ones observed numerically, highlighting the discrepancies in terms of thrust already observed between the test and simulations. The computations of DLR and IAG capture well the slop when the blade approaching the microphone, but mismatch the slop when the blade pass away the microphone. The variation of the high frequency is relative weaker

which could be attribute to the rotor broadband noise or some contamination due to reflections from the microphone support structure, etc.

Figure 15 compares predicted sound pressure spectra for two frequency ranges. For both the simulations and test, the rotor harmonic sound components are found to dominate at low frequency. Broadband noise becomes more important in the test for frequencies greater than 2 kHz, but the contribution to overall sound pressure level can be neglected. It should be mentioned that broadband sound and motor noise contributions were not included in numerical simulations.

Figure 15 shows all numerical simulations match very well the experimental trends, in which the highest level in the spectrum is located at the first BPF and decays almost linearly with increasing frequencies. The subharmonics among two BPFs observed in the experiment are caused by the influence of blade asymmetry and the motor noise. As all CFD simulations consider the blade asymmetry, the subharmonics are also captured.

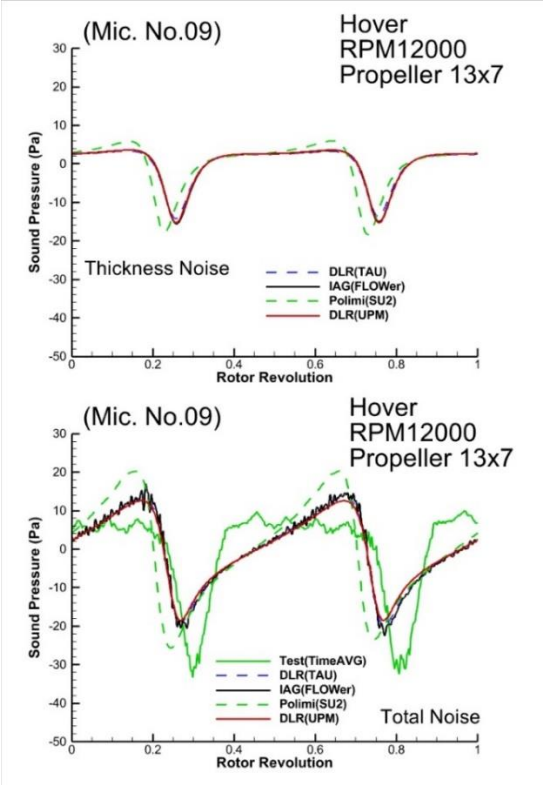

Figure 14 Time histories at Mic. position 9 for RPM 12000. Up: thickness noise;Low:total noise

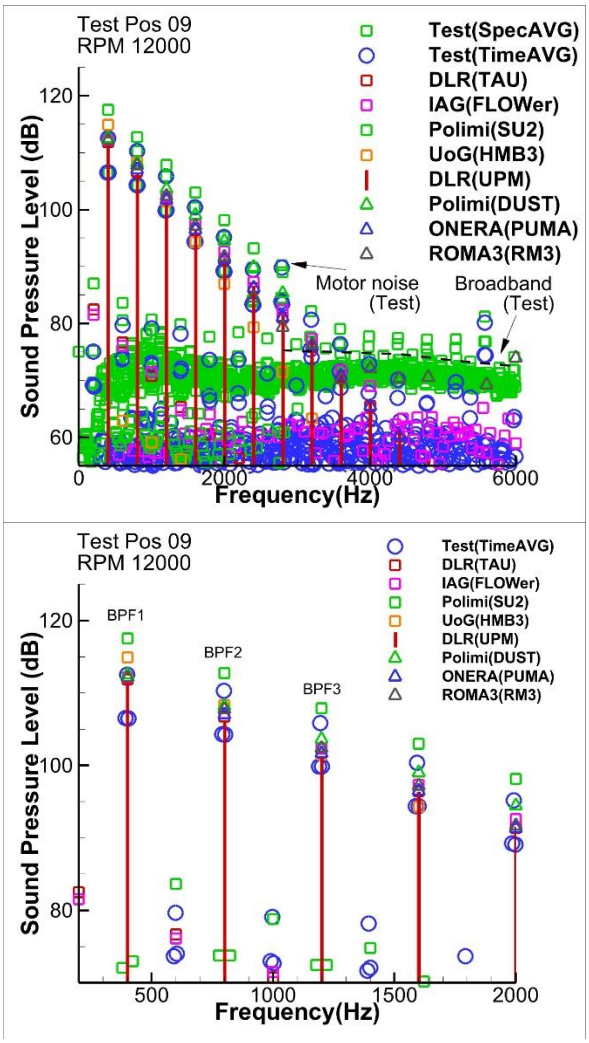

Figure 15 Sound pressure level (SPL) spectra from the microphone located at 9 for 12000rpm

5. RESULTS TWO ROTORS IN COAXIAL CONFIGURATION

For the coaxial configuration, as shown in Figure 2 and Figure 5b, the distance between two rotors is defined by ΔZ/D, where D is the diameter of the rotor in 0.33m. Both rotors are turn in opposite direction with the same rotational speed. The lower rotor defined as rotor 1, right-handed rotor (RHR) rotates counter-clockwise as for the isolated condition and the upper rotor defined as rotor 2, left-handed rotor (LHR) rotates then clockwise. The starting phase positions of the reference blade for both rotors point towards the downstream and both rotors are phase locked in the simulations. In the test however, there is no phase synchronization of the two rotors.

5.1. Hover at RPM=8000 and Δz/D=0.25

5.1.1. Aerodynamic performance

A comparison of the measured and simulated time averaged rotor thrust and torque for this coaxial

configuration is given in Figure 16 together with the value from isolated rotor. The effect of the coaxial configuration shows a decrement of the thrust. A clear effect on rotor 1, lower rotor (RHR) for both the test and all simulations (marked as red symbols) shows a larger loss of the thrust, comparing with rotor 2 LHR. This behaviour is mainly due to the effect of the upper rotor downwash which spanwise increases the induced velocity and, thus reducing the effective angles of attack.

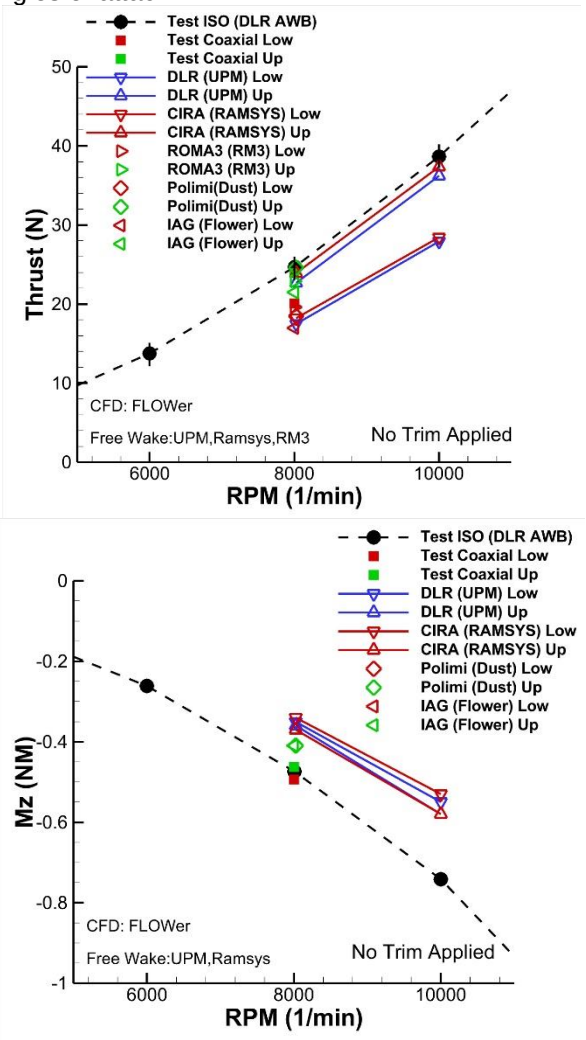

Figure 16 Time averaged rotor thrust and torque at coaxial configuration for 10000RPM

5.1.2. Ensemble Average Velocity Fields

The ensemble average velocity fields from measurement for the coaxial configuration with Δz = 0.5 R at Ω = 8025 RPM is given in Figure 17. As for the isolated case, the mean data is obtained averaging on a set of 500 instantaneous velocity map. The PIV measurement foresaw that the upper rotor was free to rotate while the lower was phase locked at rotor azimuthal position of $\Psi = 90°$ to avoid blade laser reflection in the measurement region. The mean velocity field shows the typical wake contraction downstream the lower Rotor 1 (RHR) similar to the isolated rotor (Figure 11).

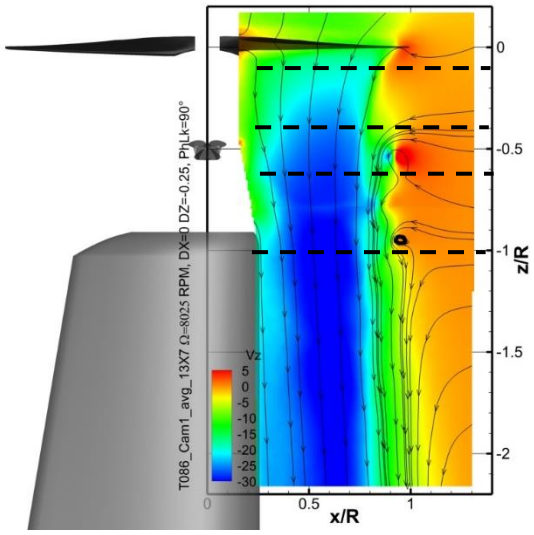

Figure 17 Iso-contours with streamtraces of the ensemble-average flow field colour-coded with the velocity vertical component for the coaxial configuration with Δz = 0.5 R at Ω = 8025 RPM

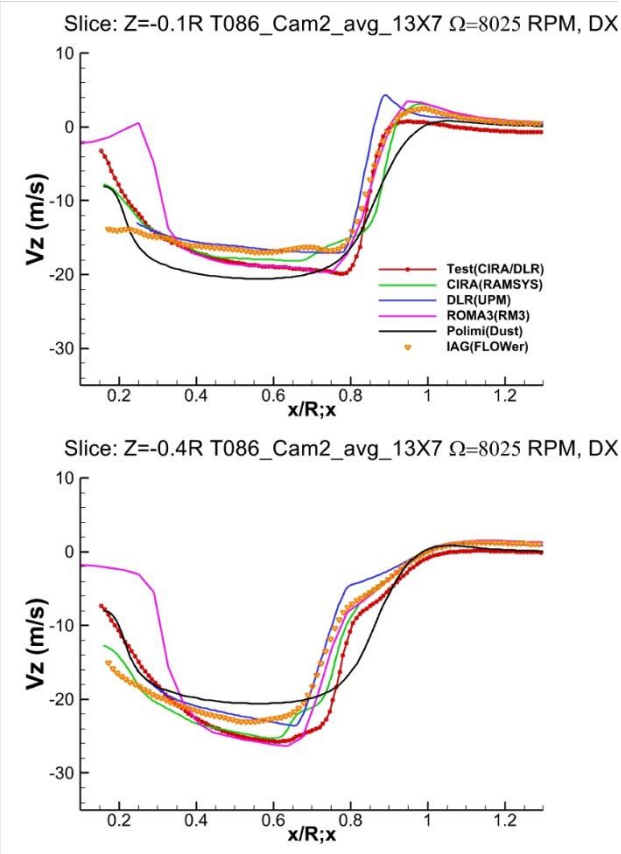

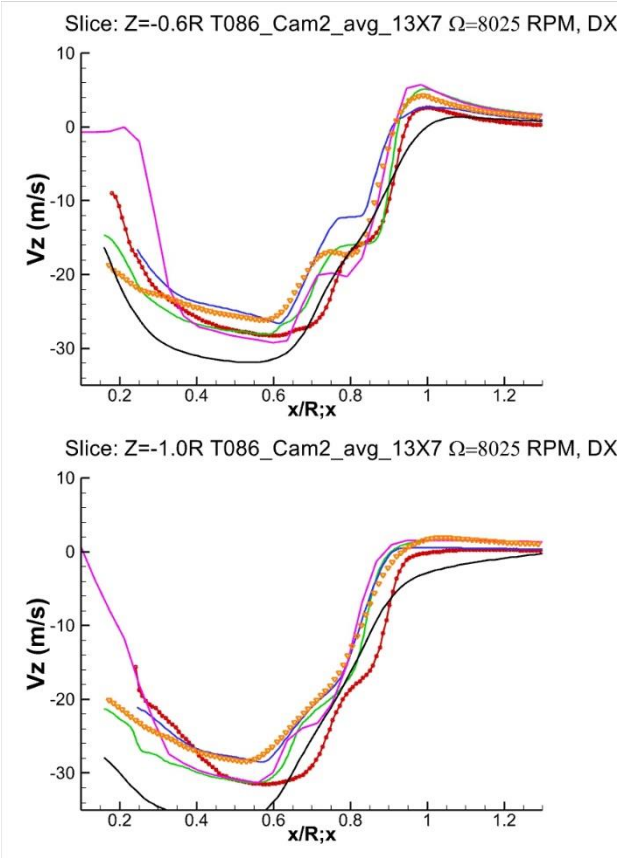

Figure 18 Vertical velocity trend along radial distance at Ω = 8025 RPM for different z-stations

Figure 18 depicts the comparisons on several slices at different Z positions marked as dashed line in Figure 17. It shows similar characteristics of the flow field demonstrated in isolated rotor case, except in the lower slice positions, basically from z/R=-0.5 downward, where more dynamic variations in the shear layer region are observed. Those dynamic variations are produced by the additional velocity induced by the lower propeller and are captured by all simulations with some variation in positions. IAG CFD Flower results has the same shear layer slope of the measurements but shifted and underestimates the maximum vertical velocity. CIRA and Rome3 presented shifted shear layer, but the same slope and induced velocity. DLR-UPM has similar behaviour to Rome3 and CIRA but slightly underestimates the induced velocity. The poor vortex dissipation is observed in Polimi-Dust.

5.1.3. Aeroacoustics

The presentation of the acoustic results will focus on data represented by microphones on a line of array from number 0 to 5 as defined in Figure 19. The microphones are located in the X-Y plane with equal distance of 0.3m to X-Z plane.

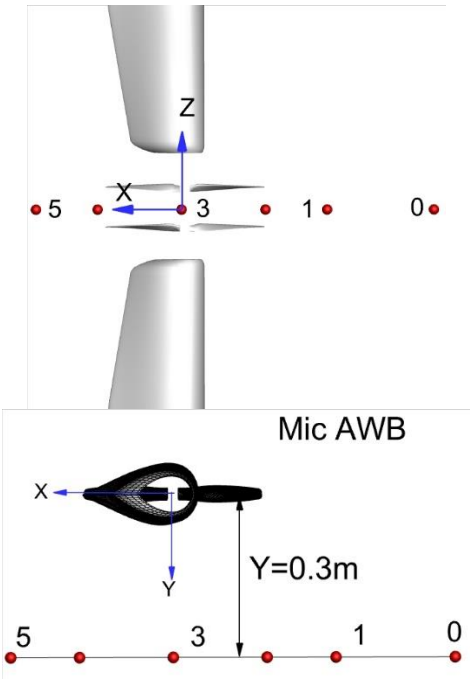

Figure 19 Microphone positions for the coaxial rotor case

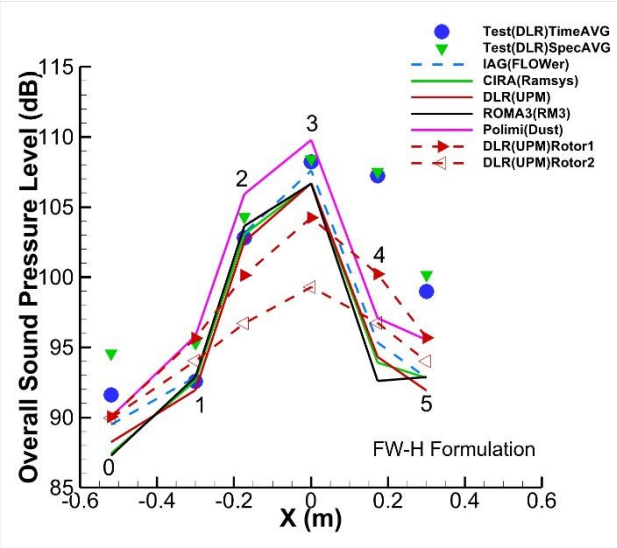

Figure 20 OASPL directivity taken from Mic 0 to Mic 5) for RPM 8000

The OASPL directivity calculated by DLR, IAG, CIRA and ROMA3 shows very good agreement for all microphones although the comparisons involve two fidelity levels. Polimi results display the highest level among the simulations. All the simulations capture the trend of the directivity. Good comparisons also observed for the microphones located at positions X<=0, but large deviations from the test results for the microphones located at X>0 are observed. In order to see the contributions from individual rotors, the comparison of the individual rotor contributions from DLR simulations also included in the plot. The noise level from lower rotor 1 is in general higher than

that from the upper rotor 2. The higher rotor 1 noise is caused possibly by higher non-uniform inflow introduced by the multi-inductions of the upper rotor 2 wake as well as the difference of the noise directivity. When comparing sum of two rotor noise with the individual contributions, the acoustic interferences are well visible, indicating for example clear noise cancelation for the microphones located at X>0. Due to slight asynchronization of RHR and LHR in the measurement, this phenomenon is not able to be measured.

Selected acoustic spectra obtained at two microphone positions (M3 and M4) are compared with the spectral-averaged test results, as shown in Figure 21. The spectral-averaged test data are chosen to better emphasize the relative importance of both the broadband and tonal components of the source.

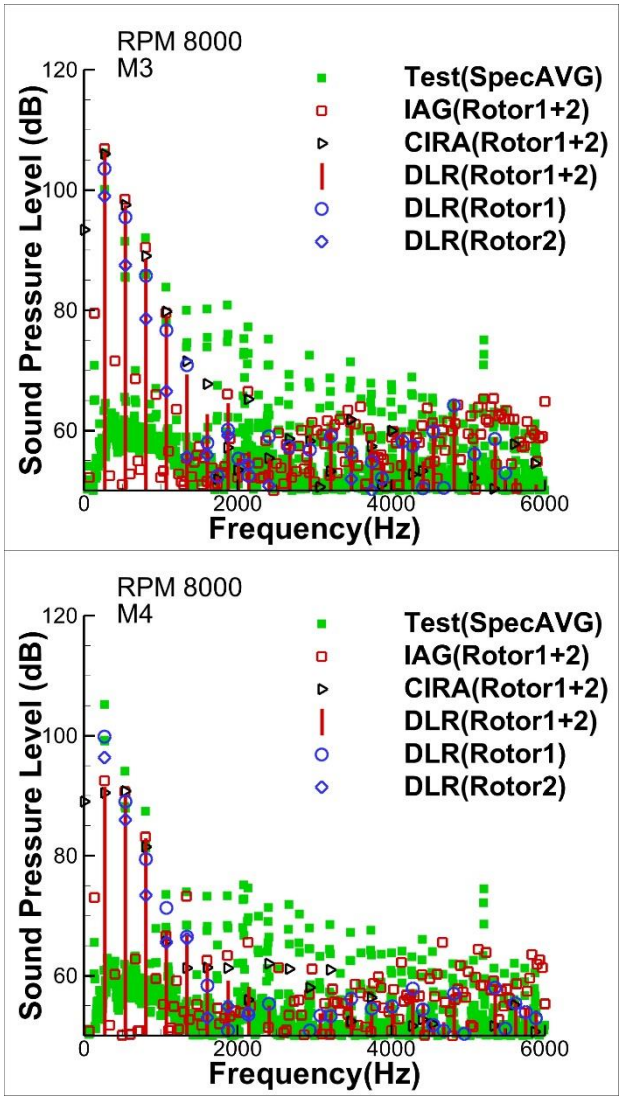

Figure 21 Sound pressure level (SPL) spectra from the microphone located at 3 and 4 for 8000rpm

For the microphone located at M3, the low frequency BPF harmonics are the dominant source of noise and Rotor 1 (RHR) noise is dominant contributor to the SPL, according to DLR simulation. In the test results, there is a clear increase in tonal component levels from the 3rd BPF harmonics and sub-harmonics upward. The increase in higher harmonic tonal component levels in the test may indicate more interactions related unsteadiness especially blade leading edge interaction with as observed in [7], which indicates a wider part of the blade will interact with the high-intensity part of the incoming turbulent flow caused partly by wandering of the tip vortex center. In addition, an effect of the unsynchronized speed in the experiment.

For the microphone located at M4, where large deviation from the test is observed, the test result shows BPF1 is dominant tone and large difference from the numerical simulations mainly occurs for this tone. This can be partly caused by the coherent summation used by the sum of two rotor components in the simulations. As indicated in BPF1, the sum of the contribution of the rotor 1 and 2 causes a reduction of the overall SPL due to the coherent effect. As mentioned, this phenomenon is not able to be measured due to slight asynchronization of the rotors in the measurement.

All the numerical simulations demonstrate good agreement for first 3 BPF tones. There is slightly high harmonic contribution above 2000Hz in IAG CFD results, which believe to be pure numerical artifacts.

6. RESULTS OF TWO ROTORS IN TANDEM CONFIGURATION

For the tandem configuration, as shown in Figure 5-a, the distance between two rotors is defined by ΔZ/D and ΔX/D, where ΔZ/D=0.25 and ΔX/D=1.18 is chosen. Similar to the coaxial case, the lower rotor defined as right-handed rotor (RHR) rotates count-clockwise and the upper rotor defined as left-handed rotor (LHR) rotates then clockwise.

6.1. Hover at RPM=8000 and Δz/D=0.25 and ΔX/D=1.18

6.1.1. Aerodynamic performance

Figure 22 compares the measured and simulated time averaged rotor thrust and torque together with the value from isolated rotor. The effect of this tandem configuration shows two rotors both in numerical simulation and in the test have very close thrust and torque values. The thrust slightly lower than isolated one. All codes predict a slightly high torque value. There is no clear effect of rotor-rotor interaction observed in the averaged performance value of the coaxial configuration.

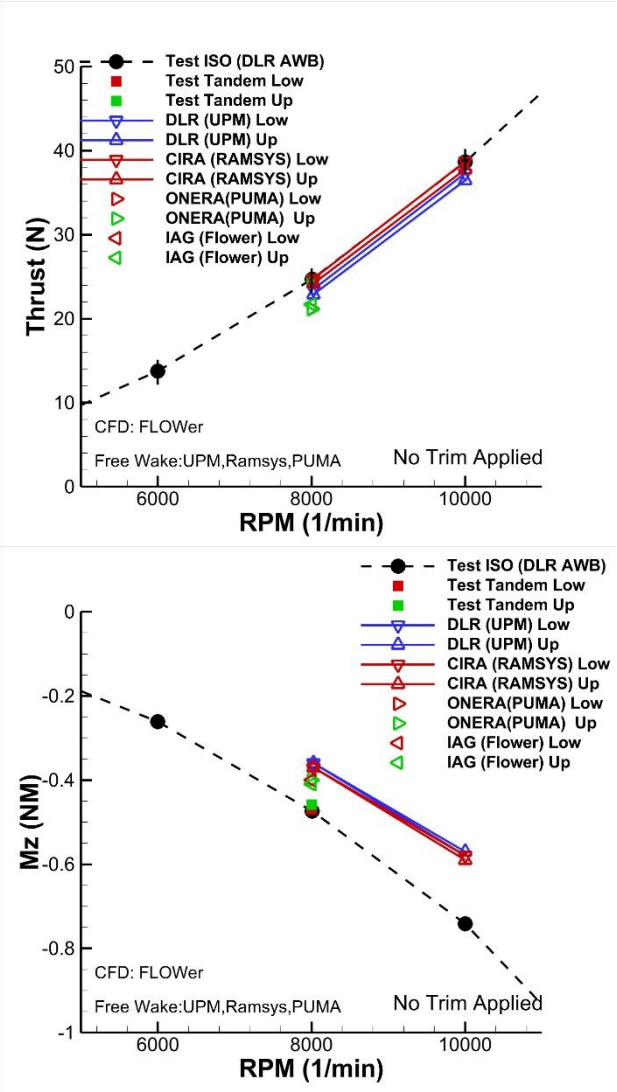

Figure 22 Time averaged rotor thrust and torque at coaxial configuration for 10000RPM

6.1.2. Ensemble Average Velocity Fields

The ensemble average velocity fields from measurement for this tandem configuration at Ω = 8025 RPM is given in Figure 23. The results were obtained on 500 instantaneous velocity fields recorded avoiding any lock between the camera acquisition frequency and the rotor speed

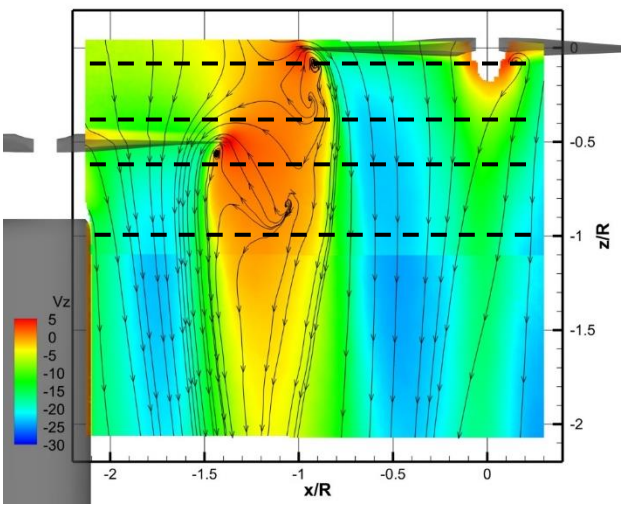

Figure 23 Iso-contours with streamtraces of the ensemble-average flow field colour-coded with the velocity vertical component for the coaxial configuration with Δz = 0.5 R at Ω = 8025 RPM

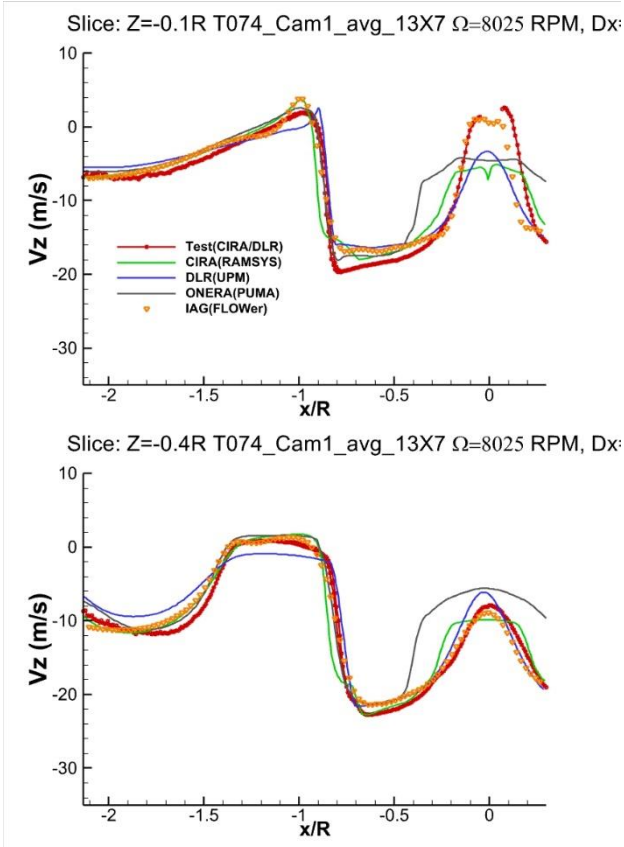

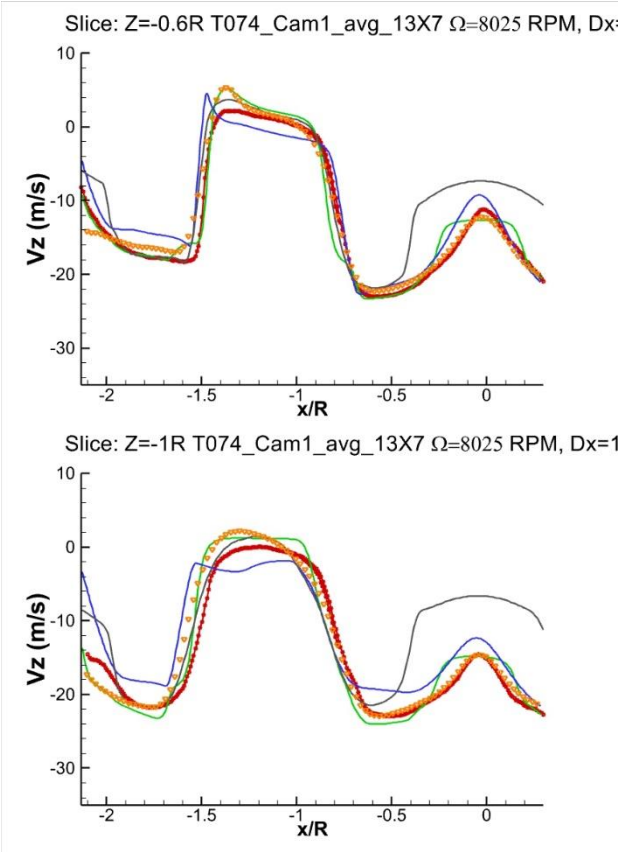

Figure 24 Vertical velocity trend along radial distance at Ω = 8025 RPM for different z-stations

For the tandem configuration, a better agreement in comparing with the coaxial condition between simulation and experiments is obtained. The plateau at x/R=0 is related to the modelling of the rotor hub which has been explained in previous section. The shear layer location is almost correct.

6.1.3. Aeroacoustics

Similar to the coaxial case, the acoustic results will be presented on a line of array from number 4 to 12 as defined in Figure 25. The microphones are located in the X-Y plane with equal distance of 0.3m to X-Z plane.

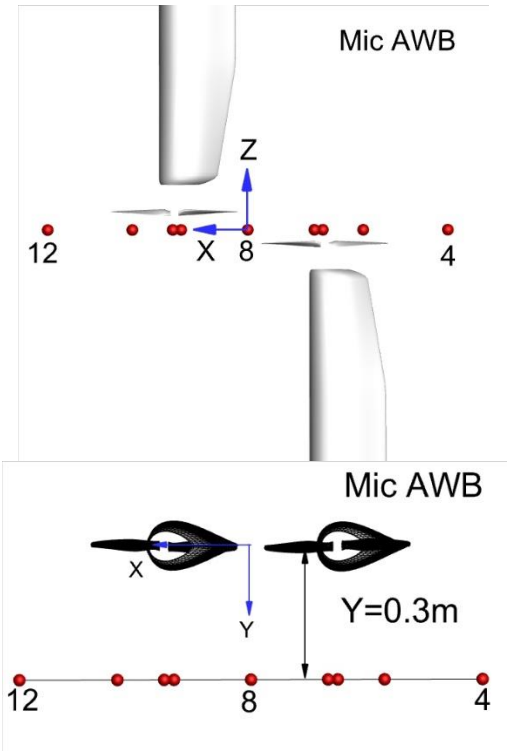

Figure 25 Microphone positions for the tandeml rotor case

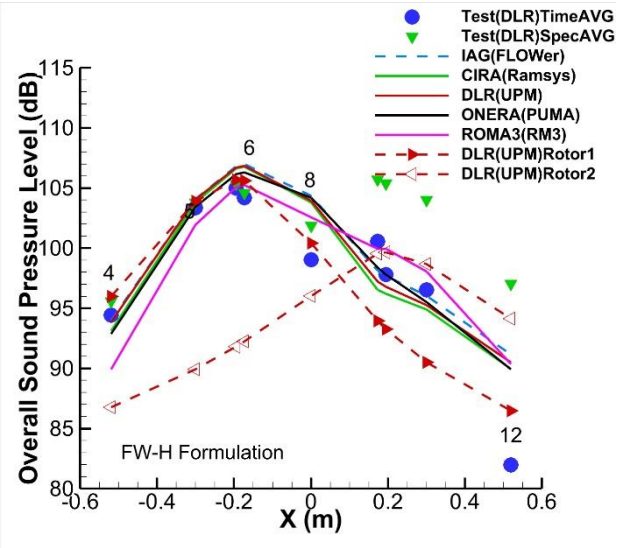

Figure 26 OASPL directivity taken from Mic 4 to Mic 12 for RPM 8000

The OASPL directivity pattern fit very well among all the simulations, except ROMA3 where higher noise around Rotor2 is observed. Good comparisons with the test also observed for the microphones located at positions close to rotor 1, except ROMA3 where lower noise around Rotor1 is observed. In comparison with the test, the deviation from the test results increases for the microphone towards the rotor 2. Large differences are also observed between time averaged and spectrum averaged test results.

To check the reason for the difference, selected acoustic spectrum obtained at two microphone positions (M6 and M8) are compared with the spectral-averaged test results, as shown in Figure 27.

For M6 and M8, the first 4 low frequency BPF harmonics are the dominant source of noise. For these 4 BPFs, the Rotor 1 (RHR) noise is the dominant contributor to the noise level for these selected microphones.

The large difference due to the interference effect between the simulation and test for first BPF is observed. The interference effect may not be captured as discussed before.

All the numerical simulations given in Figure 27 demonstrate good agreement for first 5 BPF tones.

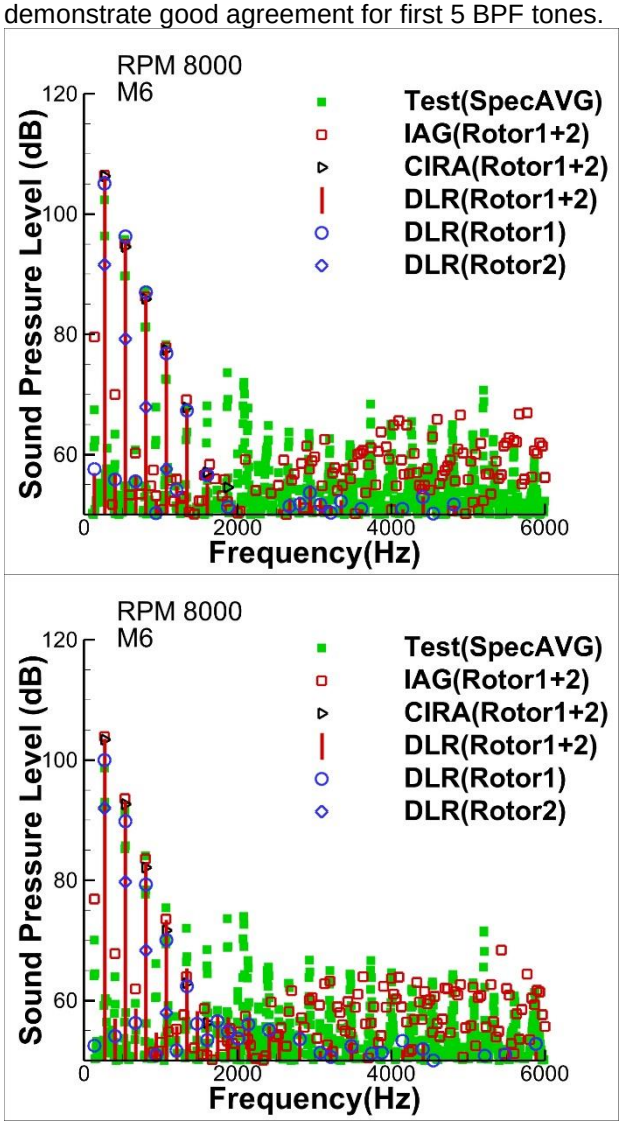

Figure 27 Sound pressure level (SPL) spectra from the microphone located at 6 and 8 for 8000rpm

7. CONCLUSION

In this paper, the wind tunnel test and the numerical activities achieved in the GARTEUR AG26 is introduced. The experimental and numerical investigations of the rotor in isolated, coaxial and tandem configuration are presented.

Comparisons of code-to-code and the code-to-test results were carried out. The test results are derived from the test carried out from CIRA/DLR PIV and DLR acoustic test. The numerical comparisons were conducted among different solvers available within GARTEUR Action Group AG26.

Both aerodynamic and aeroacoustic simulation indicate that measurement results in terms of rotor performance, flow field and acoustic divitites for most cases were reproducible and the comparison of the simulations and the test give satisfactory agreement by all computational methods, regardless of their fidelity level.

8. ACKNOWLEDGMENTS

The research leading to the presented results has been addressed within the framework of the HC/AG-26, supported by GARTEUR. POLIMI authors gratefully acknowledge the high-performance computing resources provided for this collaborative effort under the supervision of Professor Matteo Parsani by the Supercomputing Laboratory at King Abdullah University of Science & Technology (KAUST) in Thuwal, Saudi Arabia.

9. REFERENCES

[1]. Yin, J., De Gregorio, F., Petrosino, F., Rossignol, K-S, Schwarz, T., Cotte, B., Brouwer, H., Clero, F., Mortain, F., Reboul, G., Zanotti, A., Vigevano, L., Gibertini, G., Bernardini, G., Schmähl, M., Kaltenbach, H-K., Pagliaroli, T., Keßler, M., Barakos, G., Ragni, D., Testa, C.: Noise Radiation and Propagation for Multirotor System Configurations. In: Terms of Reference for the GARTEUR Action Group HC/AG-26, December 2021.

[2]. Rossignol, K.-S., Yin, J., Rottmann, L.: Investigation of Small-Scale Rotor Aeroacoustic in DLR's Acoustic Wind Tunnel Braunschweig, in 28th AIAA/CEAS Aeroacoustics 2022 Conference., Southampton, UK, 2022.

[3]. Yin, J., Rossignol, K.-S., Rottmann, L., Schwarz, T.: Numerical Investigations on Small-scale Rotor Configurations with Validation using Acoustic Wind Tunnel Data. In: 48th European Rotorcraft Forum (ERF), 2022, Seiten 1-17. 48 European Rotorcraft Forum (ERF) 2022, 6.- 8. September 2022, Winterthur, Switzerland.

[4]. Nargi, R.E., F. De Gregorio, P. Candeloro, G. Ceglia, and T. Pagliaroli 2021. Evolution of flow structures in twin-rotors wakes in drones by time-

resolved PIV. In Journal of Physics: Conference Series, Volume 1977, pp. 012008.
[5]. Ceglia, G., Nargi R.E., Candeloro P., Pagliaroli, T., De Gregorio, F., “Time-resolved PIV measurements of the rotor wake in a side-by-side configuration” 15th International Symposium on Particle Image Velocimetry, San Diego, CA, June 2023.
[6]. Zanotti, A. and Algarotti, D., “Aerodynamic interaction between tandem overlapping propellers in eVTOL airplane mode flight condition,” Aerospace Science and Technology 124: 107518, 2022.
[7]. F. De Gregorio Rossignol, K.-S., G. Ceglia, J. Yin.: Multi-rotor wake interaction characterization. 49 European Rotorcraft Forum (ERF) 2023, 5.- 7. September 2023, Bückeburg, Germany.
[8]. M. Pott-Pollenske, J. W. Delfs, “Enhanced Capabilities of the Aeroacoustic Wind Tunnel Braunschweig”, 14th AIAA/CEAS Aeroacoustics Conference (29th AIAA Aeroacoustics Conference), 2008, AIAA-2008-2910
[9]. Raffel M., Willert C. E., Wereley S. T., and Kompenhans J. (2007) Particle Image Velocimetry - A Practical Guide, Springer-Verlag Berlin Heidelberg, 2nd edition doi: 10.1007/978-3-540-72308-0.
[10]. A. Visingardi, A. D'Alascio, A. Pagano, P. Renzoni, Validation of CIRA's rotorcraft aerodynamic modelling system with DNW experimental data, in: 22nd European Rotorcraft Forum, Brighton, UK, 1996. doi: http://hdl.handle.net/20.500.11881/3171
[11]. Morino, L., “A General Theory of Unsteady Compressible Potential Aerodynamics,” NASA CR-2464, 1974.
[12]. J. E. F. Williams, D. L. Hawkings, Sound generation by turbulence and surfaces in arbitrary motion, Philosophical Transactions of the Royal Society of London. Series A, Mathematical and Physical Sciences 264 (1151) (1969) 321{342. URL http://www.jstor.org/stable/73790
[13]. D. Casalino, An advanced time approach for acoustic analogy predictions, Journal of Sound and Vibration 261 (4) (2003) 583{612. doi: https://doi.org/10.1016/S0022-460X(02)00986-0.
[14]. D. Casalino, M. Barbarino, A. Visingardi, Simulation of helicopter community noise in complex urban geometry, AIAA Journal 49 (8) (2011) 1614{1624. doi:10.2514/1.J050774.
[15]. M. Barbarino, F. Petrosino, A. Visingardi, A high-fidelity aeroacoustic simulation of a VTOL aircraft in an urban air mobility scenario, Aerospace Science and Technology (2021). 107104. 10.1016/j.ast.2021.107104.
[16]. S.R. Ahmed, V.T. Vidjaja, “Unsteady Panel Method Calculation of Pressure Distribution on BO105 Model Rotor Blades“, Journal of the American Helicopter Society, pp. 47-56, Jan. 1998.
[17]. J. Yin, S.R. Ahmed, “Helicopter main-rotor/tail-rotor interaction”. Journal of the American Helicopter Society, Vol. 45 (No. 4), pp. 293 -302, 2000.
[18]. D. Schwarmborn, T. Gerhold, R. Heinrich, “The DLR TAU-Code: Recent Applications in Research and Industry”, Proceedings of European Conference on Computational Fluid Dynamics ECCOMAS CFD 2006, Delft, Netherlands.
[19]. J. Yin, B.G. van der Wall, G.A. Wilke “Rotor Aerodynamic and Noise under Influence of Elastic Blade Motion and Different Fuselage Modeling”. 40th European Rotorcraft Forum (ERF) 2014, 2-5 September 2014, Southampton, UK.
[20]. M. Mudry, “La théorie des nappes tourbillonnaires et ses applications à l’aérodynamique instationnaire,” PhD thesis, University of Paris VI, July 1982.
[21]. R. Boisard, “Numerical Analysis of Rotor / Propeller aerodynamic interactions on a high-speed compound helicopter”, Journal of the American Helicopter Society, Volume 67, Number 1, January 2022, pp. 1-15, DOI: 10.4050/JAHS.67.01200
[22]. L. Cambier, S. Heib, and S. Plot, “The ONERA elsA CFD software: input from research and feedback from industry,” Mechanics & Industry, Vol. 14, (3), 2013, pp. 159–174.
[23]. J. Prieur and G. Rahier, “Comparison of the Ffowcs Williams-Hawkings and Kirchhoff rotor noise calculations”. 4th AIAA/CEAS Aeroacoustics Conference, Toulouse, 1998.
[24]. G. Rahier and J. Prieur, “An efficient Kirchhoff integration method for rotor noise prediction starting indifferently from subsonically or supersonically rotating meshes” 53rd AHS Annual Forum, Virginia Beach, USA, 1997.
[25]. Tugnoli, M., Montagnani, D., Syal, M., Droandi, G., and Zanotti, A., “Mid-fidelity approach to aerodynamic simulations
[26]. of unconventional VTOL aircraft configurations,” Aerospace Science and Technology, Vol. 115, 2021, p. 106804. https: //doi.org/10.1016/ j.ast.2021.106804.
[27]. Economon, T. D., Palacios, F., Copeland, S. R., Lukaczyk, T. W., and Alonso, J. J., “SU2 An open-source suite for multiphysicsì simulation and design,” AIAA Journal, Vol. 54, No. 3, 2016, pp.828–846. https://doi.org/10.2514/1.J053813.
[28]. Galimberti, L., Morelli, M., Guardone, A., and Zhou, B. Y., “Propeller Noise Prediction Capabilities within SU2,” Proceedings of the

AIAA SCITECH 2023 Forum, National Harbor, MD & Online, 2023, p. 1548. https://doi.org/10.2514/6.2023-1548.

[29]. Gennaretti, M., Bernardini, G., Serafini, J., & Romani, G. (2018). Rotorcraft comprehensive code assessment for blade–vortex interaction conditions. Aerospace Science and Technology, 80, 232-246.

[30]. Gennaretti, M., Colella, M. M., and Bernardini, G., "Prediction of tiltrotor vibratory loads with inclusion of wing-proprotor aerodynamic interaction," Journal of Aircraft, Vol. 47, No. 1, 2010, pp. 71–79.

[31]. Gennaretti, M., and Bernardini, G., "Novel boundary integral formulation for blade-vortex interaction aerodynamics of helicopter rotors," AIAA journal, Vol. 45, No. 6, 2007, pp. 1169–1176.

[32]. Ffowcs Williams, J.E., and Hawkings, D.L., 'Sound Generation by Turbulence and Surfaces in Arbitrary Motion,' Philosophical Transactions of the Royal Society, Vol. A264, No. 1151, 1969, pp. 321-542.

[33]. Farassat, F., "Derivation of Formulations 1 and 1A of Farassat," 2007.

[34]. Kroll, N., Rossow, C. C., Becker, K. and Thiele, F., MEGAFLOW-a numerical flow simulation system,} 21st ICAS congress, Melbourne, Austrila, Sep. 1998, pp. 09–13.

[35]. Keßler, M., Frey, F., Letzgus, J., Ohrle, C., Thiemeier, J. and Krämer, E., Progress in IAG's Rotorcraft Simulation Framework, High Performance Computing in Science and Engineering '20, Springer International Publishing, 2021, pp. 331--341. ISBN: 978-3-030-80602-6

[36]. Keßler, M., and Wagner, S., Source-Time Dominant Aeroacoustics, Computers & Fluids, Vol. 33, 2004, pp. 791–800.

[37]. Jameson, A., Time Dependent Calculations Using Multigrid, with Applications to Unsteady Flows Past Airfoils and Wings, AIAA 10th Computational Fluid Dynamics Conference, Honolulu, Hawaii, June 1991. DOI: 10.2514/6.1991-1596

[38]. Borges, R., Carmona, M., Costa, B. and Don, W. S., An Improved Weighted Essentially Non-Oscillatory Scheme for Hyperbolic Conservation Laws, Journal of Computational Physics, Vol. 227, (6), March 2008, pp. 3191--3211. DOI: 10.1016/j.jcp.2008.11.038

[39]. Steijl, R., Barakos, G., and Badcock, K., "A framework for CFD analysis of helicopter rotors in hover and forward flight," International journal for numerical methods in fluids, Vol. 51, No. 8, 2006, pp. 819–847.

[40]. Biava, M., Woodgate, M., and Barakos, G. N., "Fully implicit discreteadjoint methods for rotorcraft applications," AIAA Journal, Vol. 54, No. 2, 2016, pp. 735–749.

[41]. Antoniadis, A., Drikakis, D., Zhong, B., Barakos, G., Steijl, R., Biava, M., Vigevano, L., Brocklehurst, A., Boelens, O., Dietz, M., et al., "Assessment of CFD methods against experimental flow measurements for helicopter flows," Aerospace Science and Technology, Vol. 19, No. 1, 2012, pp. 86– 100.

[42]. Steininger, R., Barakos, G. N., and Woodgate, M. A., "Numerical Analysis of HVAB and STAR Rotor Blades Using HMB3," AIAA SCITECH 2023 Forum, 2023, p. 1189.

[43]. Babu, S., Loupy, G., Dehaeze, F., Barakos, G., and Taylor, N., "Aeroelastic simulations of stores in weapon bays using Detached-Eddy Simulation," Journal of Fluids and Structures, Vol. 66, October 2016, pp. 207–228, DOI: 10.1016/j.jfluidstructs.2016.07.014.

[44]. Barakos, G. and Johnson, C., "Acoustic comparison of propellers," International Journal of Aeroacoustics, Vol. 15, No. 6-7, 2016, pp. 575–594, DOI: 10.1177/1475472X16659214.

[45]. Qiao, G., Parametric study of aerodynamic performance of equivalent ducted/un-ducted propellers based on high-fidelity computational fluid dynamics, Master's thesis, University of Glasgow,2021,http://theses.gla.ac.uk/id/eprint/82702.

[46]. Menter, F. R., "Two-equation eddy-viscosity turbulence models for engineering applications," AIAA journal, Vol. 32, No. 8, 1994, pp. 1598–1605.

[47]. Smith, D., Filippone, A., and Barakos, G., "Acoustic analysis of counterrotating open rotors with a locked blade row," AIAA Journal, Vol. 58, No. 10, 2020, pp. 4401–4414.